A Generic Three-Dimensional Static Force Distribution Basis for a Medical Needle Inserted into Soft Tissue

Adeline L.G. Robert[a,*], Grégory Chagnon[a], Ivan Bricault[b,c], Philippe Cinquin[a], Alexandre Moreau-Gaudry[a,c,**]

[a] *UJF-Grenoble1, CNRS, TIMC-IMAG UMR5525, Grenoble - France*
[b] *Service central de radiologie et d'imagerie médicale, CHU Grenoble, Grenoble, France*
[c] *UJF-Grenoble1, INSERM, CHU Grenoble, CIT803, Grenoble, France*

Abstract

In this paper, the static interaction forces between a medical needle and soft tissue during CT (Computerized Tomography) guided insertion are studied. More precisely a set of linearly independent elements describing the forces (a basis) is identified. This forms a generic basis from which any forces that act on a static needle (that is not fixed at its base and that is inserted into human tissue) can be described accurately. To achieve this purpose, the same needle was inserted 62 times into fresh porcine shoulder tissue and CT scans were acquired after each push to determine the final trajectory of the needle. From this set of trajectories, a generic static force basis was determined by using static Beam, B-spline theories and Principal Component Analysis (PCA). This generic basis was first validated on theoretical simulations and then on 20 different needles inserted into in-vivo human tissues during real clinical interventions. Such a basis could be of use to highlight the forces acting all along the length of a needle inserted into a complex tissue and enables models of needle deflection to be developed. These models could be

[☆] A clinical trial was performed at Grenoble University Hospital involving CT-guided interventional radiological procedures such as biopsies, injections etc. The clinical trial was authorized by AFSSaPS (now ANSM), the relevant French regulatory authority for biomedical research and by the Comité de Protection des Personnes Sud-Est V, a French institutional review board (ClinicalTrials.gov identifier: NCT00828893).

[*] Principal corresponding author
[**] Corresponding author
Email addresses: Adeline.Robert@imag.fr (Adeline L.G. Robert), Alexandre.Moreau-Gaudry@imag.fr (Alexandre Moreau-Gaudry)

used in the development of automated robot assisted and/or image guided strategies for needle steering.

Keywords: Needle deformation, Force distribution, Ex-vivo measurements, In-vivo forces, B-spline theory, Beam theory

---

1. Introduction

Many medical interventions involve the insertion of needles to perform a diagnostic or therapeutic act. Such percutaneous insertions into soft tissues are one of the most common minimally invasive procedures. Among the primary imaging techniques used in interventional radiology to obtain the needle and target positions, CT is of particular interest. It enables the clinical radiologist to view any part of the body in three-dimensions and with typically higher definition than other means of imagery. Hence, CT-guidance has become a well-established technique for percutaneous needle procedures. Among the different CT-guidance techniques, one is commonly used. This consists in pushing the needle stepwise into the body towards a predefined CT-target and a control CT-image is performed after each elementary push. These control images are made to check that the needle is effectively moving towards the target without unintentionally damaging surrounding tissue. It should be noted that the trajectory of the needle may be complex and not necessarily straight, with the needle undergoing deformation due to its interactions with inhomogeneous tissues and organs. In clinical practice, these control images are made when the needle is motionless and not held at the proximal end. To better understand the real interactions between a needle and living tissues in this static state, we therefore focused on this control step commonly encountered in CT-guided clinical practice.

Understanding the forces involved in needle-tissue interactions remains a real challenge. For instance, in percutaneous interventions, for several reasons characterization of the contact mechanism between the surgical needle and organs is complex (Podder et al., 2006b; Abolhassani et al., 2007; Barbe et al., 2007). These reasons include the different characteristics of the various layers of tissues encountered by the needle (fat, muscle etc), the dependence of their biomechanical properties on the patient (age, disease etc) and the properties of the needle itself. Several authors have considered the forces

involved during the dynamic insertion of a needle (Kataoka et al., 2002; DiMaio and Salcudean, 2002; Okamura et al., 2004; Washio et al., 2004; Crouch et al., 2005; Podder et al., 2006; Hing et al., 2007; Misra et al., 2008; Roesthuis et al., 2011) as shown in figure 1(a), and as a function of insertion depth. Furthermore, for most of the forces considered (Simone and Okamura, 2002; Dehghan et al., 2008; Abayazid et al., 2011; Asadian et al., 2012), the associated parameters of the model have to be fitted using experimental data from previous insertions.

Contrary to works described in the literature, our study focuses on a succession of static insertion situations. Unlike dynamic insertion approaches, the consequences are the disappearance of axial and frictional forces as shown in figure 1(b). A method using Beam and B-Spline theories is used to analyze the static forces along the needle during the stages of its insertion into soft tissue. A Principal Component Analysis (PCA) is used to identify the principal modes and thus the principal forces, responsible for the plausible variations in the needle trajectories. A generic set of linearly independent elements (a basis) describing the static forces is thus obtained from which any forces that act on a needle statically inserted into human tissue may be decomposed accurately. To the best of our knowledge, the description of the basis describing the static forces acting on the entire length of the needle and then its validation in in-vivo human tissues has not been previously presented.

This basis will be useful to simulate, in realistic way, any static needle-tissue interactions that may be encountered in clinical practice. It may also be useful to optimize the design of instrumented needles (ie, needles fitted with sensors or strain gauges) currently in development to display the real trajectory of the needle (Park et al., 2010; Yang et al., 2010).

Our work is divided into three parts. In the first part, the methodology and materials to analyze the static force basis are presented. In the second part, criteria and results for validating the static force basis are given. In the third part, a discussion of the method and results is provided. Finally, some concluding remarks close the paper.

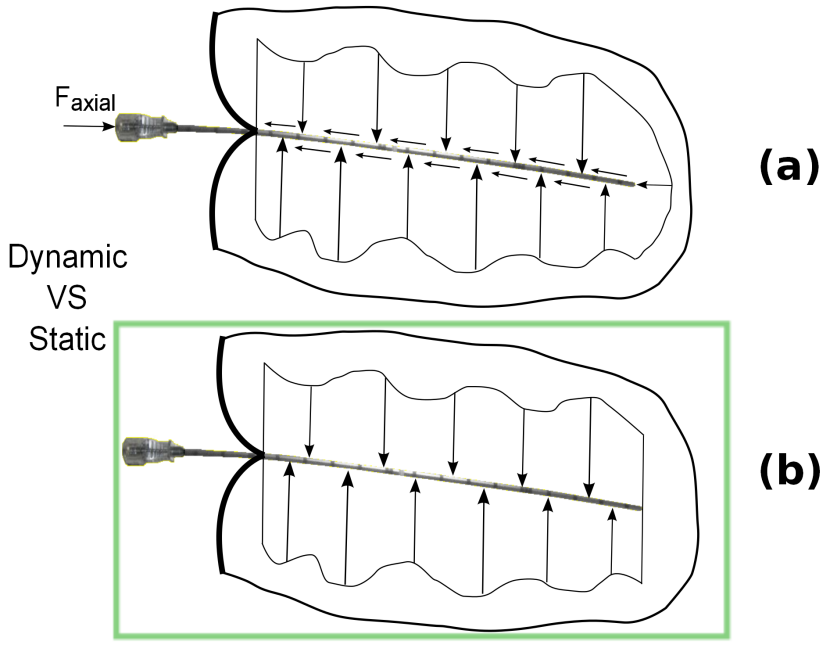

Figure 1: Forces applied to a needle. *a*) Dynamic insertion assumptions, *b*) static insertion assumptions. Contrary to the dynamic insertion assumption model, the axial and friction forces are no longer taken into account in the static model.

2. Methods and Materials

Firstly, the methodology used to analyze the distorsion of the needle shape is described and a description of data registration is given. Some elements of mechanical beam theory that are pertinent to this work are presented. Convenient notions about B-splines are then described for modeling the needle deformations. Finally, the principles of the PCA approach applied to B-splines are shown.

Secondly, the tools and materials used during the different experiments (insertion into porcine shoulder tissue, theoretical simulation and clinical cases) are described.

2.1. Methods

2.1.1. Synthesis of study methodology

To study the forces exerted on a needle, one commonly used type of needle was considered and its deflections were analyzed when it was inserted into ex-vivo porcine tissue (pig shoulder). First, all needle deflections were registered in order to make them comparable. Second, all needle deflections were modeled by B-splines. Then, by associating the B-spline and beam theories, the bending moment and shear forces along the needle were computed. Finally, a statistical approach was employed to extract the pertinent information from the set of deflections including bending moment and shear forces. This generic 3D force basis could then be used to reconstruct any needle deflection through beam theory and a linear combination of independent force vectors.

2.1.2. Spatial registration of data

CT scans of the needle trajectories were acquired on a Siemens 16 channel MDCT instrument (B30f body kernel, 2 mm slice thickness). The needle deflection was obtained using specially developed software, which makes it possible to segment manually and record points in space with a reconstruction interval of 0.1 mm (by interpolation of the CT slices) as shown in figure 2(a) and 3 (blue crosses represent the segmented needles). Furthermore, from a set of CT images with a slice thickness of $2mm$ and a CT resolution of $0.6mm$ (1.5 pixel per mm), this software allows us to work with a better sampling of the images. The slice thickness becomes $0.1mm$ (by interpolation of the CT slices) and the coordinates of points in the CT images have a precision of $0.001mm$.

In order to register all the trajectories, a common reference frame was defined as illustrated in figure 2(b). Its origin O corresponds to the proximal extremity of the needle, which is usually held by the plastic hub. The x-axis was defined by the straight line, parallel to the line fitted with a least-squared method on the segmented points and including the origin O. Then by specifying the plane with a least squares method including the x-axis, the total reference frame was built. Two orthogonal planes were defined. The first, called $P1$ (Oxz), was the plane of greatest deflection (least-squared plane)

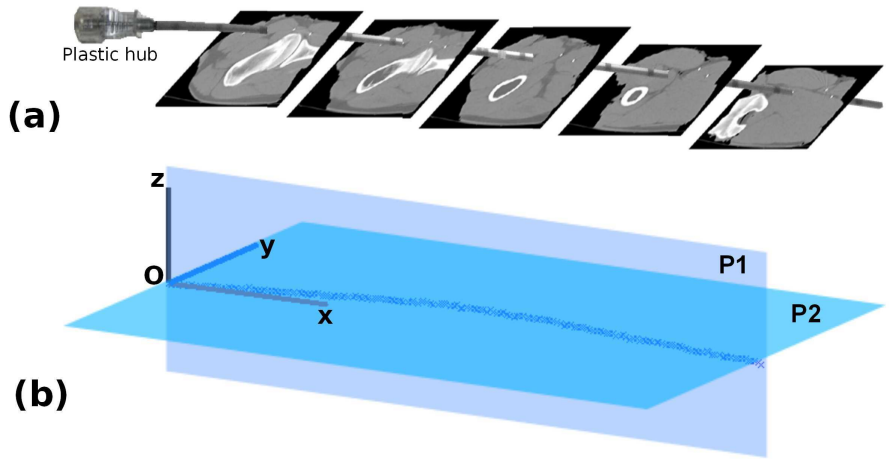

Figure 2: *a*) Needle segmentation from CT images. *b*) Visualization of the 2 orthogonal planes $P1$ and $P2$, which represent the plane of greatest deflection and the plane of the secondary curves, respectively.

and the second, called $P2$ (Oxy), was orthogonal to $P1$. The trajectories were studied in the two planes, $P1$ and $P2$. A representation of the needle trajectories projected on the two planes is shown in figure 3.

As only one needle was used to build the force basis, it was possible to normalize the basis. Thanks to this normalization, it is then possible to use it with any needle.

2.1.3. Application of Beam theory to needles

Needle can be considered as mono-dimensional structure (beams) as the length of the neutral axis is large compared to the dimensions of the cross-sections. The following two assumptions are also true for needle:

- the radius of curvature of the neutral axis is large compared to the cross-sections dimensions,
- the possible variations in the area of the cross-section are weak and progressive.

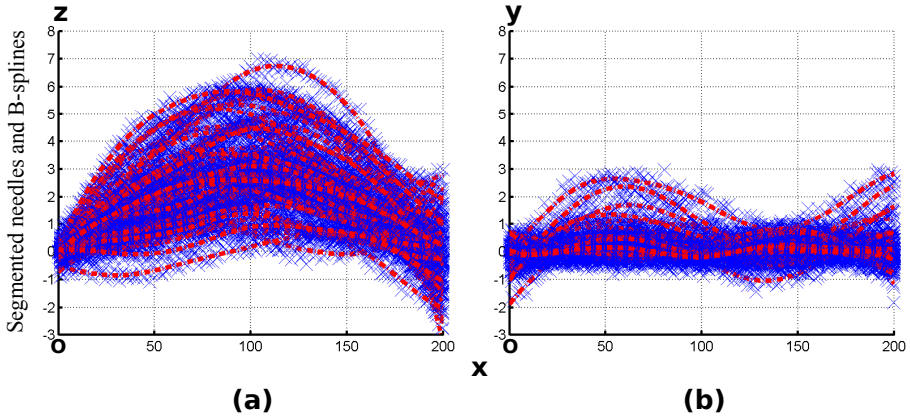

Figure 3: Registration of all needle deflections when inserted into a porcine shoulder tissues. *a*) Visualization of the deflections in the plane $P1$ (Oxz), *b*) Visualization of the deflections in the plane $P2$ (Oxy)

Beam theory is therefore an appropriate tool for studying needles and for obtaining the relationship between their deflection and the applied forces. The deflection of a needle during a medical intervention is shown in figure 4.

As the beam is made to deform, it is supposed that 1) the deformations undergone by the beam, as well as the displacements which can be measured, remain small (small deformation assumption) so that the material remains in the elastic domain, and 2) the points of external force application remain constant throughout. In fact, the tip deflection was relatively small for all the experiments (less than 10% of the needle's length) such that small-strain linear beam theory applies.

Based on these hypotheses, the bending moment-curvature beam equation can therefore be written as:

$$\gamma \approx \frac{d^2y(x)}{dx^2} = \frac{M_f(x)}{EI} \tag{1}$$

where γ is the curvature, y is the displaced position, x is the coordinate along the beam, M_f is the bending moment, E is the Young's modulus of the material and I is the second moment of area. The shear force V and the

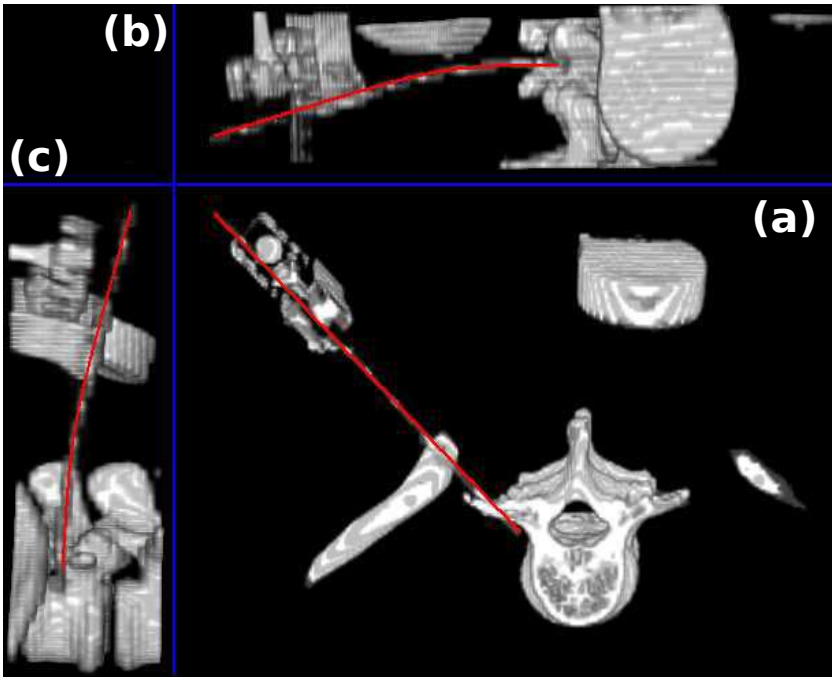

Figure 4: 3D reconstruction of a needle used in a medical intervention from CT images. *a*) Overall view of needle deflection, *b*) Sagittal section: visualization of the bending of the needle, *c*) Coronal section: visualization of the bending of the needle.

transverse force q can be deduced from the bending moment:

$$\frac{dM_f(x)}{dx} = -V(x) \tag{2}$$

$$\frac{d^2M_f(x)}{dx^2} = q(x) \tag{3}$$

2.1.4. Mathematical model

Sixty-two 3D needle deflections were used to build the generic 3D force basis. Each 3D deflection was approximated as a uniform cubic B-spline S_d ($d = 1 \dots 62$), i.e. as a linear combination of cubic B-splines. A regular grid of $n + 1$ real values t_i ($i = 0 \dots n$, with $n = 6$ in this study), called knots with $0 = t_0 < \dots < t_n = L$, was defined and the expression of S_d was:

$$\forall t \in [t_0\ t_n], S_d(t) = \sum_{i=-3}^{n-1} P_{d,i} N_{i,k}(t) \tag{4}$$

where $k = 3$ is the degree of the B-spline, $P_{d,i}$ are the control points for the d^{th} 3D needle deflection and $N_{i,k}$ are the B-splines functions, each determined starting from the preceding one by recurrence:

$$\forall t \in [t_0\ t_n], N_{i,0}(t) = \begin{cases} 1 & \text{if } t \in [t_i\ t_{i+1}] \\ 0 & \text{else} \end{cases}$$

For $k \geq 1$ and $\forall t \in [t_0\ t_n]$,

$$N_{i,k}(t) = \frac{t - t_i}{t_{i+k} - t_i} N_{i,k-1}(t) + \frac{t_{i+k+1} - t}{t_{i+k+1} - t_{i+1}} N_{i+1,k-1}(t) \tag{5}$$

S_d was also broken up into two planar cubic B-splines ($S_d^1, P_{d,i}^1, i = -3 \ldots n-1$) and ($S_d^2, P_{d,i}^2, i = -3 \ldots n-1$) in $P1$ and $P2$, respectively. The deflections S^j ($j = 1, 2$) in the j^{th} plane were:

$$\forall t \in [t_0\ t_n], S_d^j(t) = \sum_{i=-3}^{n-1} P_{d,i}^j N_{i,k}(t) \tag{6}$$

The $P_{d,i}^j$ coefficients were obtained by minimizing the following problem:

$$u_0(S_d^j(x_0^j) - y_0^j)^2 + u_1 \left(\frac{dS_d^j}{dt}(0) - dy_0^j \right)^2 + \sum_{k=1}^{m} w_k (S_d^j(x_k^j) - y_k^j)^2 + \tau \int_0^L \left(\frac{d^2 S_d^j}{dt^2}(t) \right)^2 dt \tag{7}$$

where $(x_k^j, y_k^j)_d$, $k = 0 \ldots m$ are the projections of the $(m+1)$ segmented points of the d^{th} needle in the plane Pj ($j = 1, 2$) and $x_0^j = 0$, y_0^j and dy_0^j are the information on the position and the orientation of the proximal extremity, u_0, u_1, w_k (all set at 1) and $\tau = 100$ are the weights chosen to acquire a good compromise between the smoothness of the result and the interpolated cubic B-spline.

As a result of the modeling with B-splines, the different derivatives could be computed for each new shape, thus giving access to the bending moment and the shear forces described in the paragraph 2.1.3.

2.1.5. Principal Component Analysis (PCA)

In this section, we describe the use of PCA (Cootes, 2000; Cootes et al., 2001) to build a model of the behavior of needles by analyzing the set of

shapes of such needle trajectories. This model makes it possible to extract relevant information related to this set of shapes and may mimic shapes similar to those of the 'training' set. It gives a compact representation of allowable variations, and is specific enough not to allow arbitrary variations different from those seen in this set.

Our approach requires that the topology of the object cannot change and that the object is not so amorphous that no distinct landmarks can be applied. According to paragraph 2.1.3, the needle is comparable to a beam in terms of the various mechanical assumptions required for beam theory: it does not exhibit large deformations. According to paragraph 2.1.2, needle trajectories are aligned in a common coordinate frame: these trajectories (shapes) are considered to be independent of the position and orientation of the needle and are hence comparable. Moreover, each needle trajectory is modeled by a uniform cubic B-spline according to the same methodology. This methodology guarantees the coherence of landmarks, which are defined in this work as the control points, used to define the B-splines.

Given a set of needle shapes S_d $(d = 1 \dots 62)$, and more precisely, given a set of associated control points $P_d = P_{d,i}, i = -3 \dots n-1$, a mean shape $\bar{S}$ may be defined from its mean control points $\bar{P} = \bar{P_{d,i}}, i = -3 \dots n-1$. A new set of control points P, associated to a new shape S may be approximated by:

$$P \simeq \bar{P} + Db \tag{8}$$

where $D = (D_1|D_2|...|D_p)$ contains p eigenvectors of the covariance matrix, with

$$\sum_{i=1}^{p} \lambda_i \geq 0.95 \sum_{Tot} \lambda_i \tag{9}$$

where λ_i is the eigenvalue associated with the eigenvector D_i and b is a p dimensional vector defining a set of parameters of the deformable model given by

$$b = D^T(P - \bar{P}) \tag{10}$$

2.2. Material

2.2.1. Porcine shoulder and needle (PI needle)

Porcine shoulder (ex-vivo) was selected to carry out the tests. This choice was justified by the similarity of the biomechanical properties of porcine tissue compared with human tissue, as well as the presence of tendons, muscles and bones, allowing needle insertion into a complex medium. This choice was justified by clinicians (Hocking et al., 2011), who reported that needle insertion into ex-vivo porcine tissue feels more similar to in-vivo human tissue than other ex-vivo tissues. A fresh shoulder ($300\times200\times100$ mm) was prepared and placed in a plastic case in the CT scanner. The outer wall of the muscle was free.

The needle, a type commonly used for interventional radiology procedures, was a 22 gauge stainless steel needle of length 200mm and with a material Young's modulus estimated at 200 GPa. The needle tip was beveled at an angle of 40 degrees. The needle was inserted into the tissue under a variety of different conditions for a total of 62 insertions. The conditions of insertion were as close as possible to those used in real clinical interventions, so as to explore the various possibilities for needle deflection which could take place during real percutaneous interventional radiology. For this reason, the needle was inserted manually, with no fixed velocity, with or without forcing orthogonally on the plastic hub and both with or without rotation. The different conditions used during needle insertion, intended to create variability in the resulting needle deflections, are detailed in table 1. The first column gives the number of the insertion. The conditions of insertion are specified in the second column, which could include one or two rotations after different lengths of insertion with an associated angle of rotation. The last column gives the orthogonal forces applied to the proximal extremity of the needle, which could be in line with or orthogonal to the bevel, to highlight the influence of the bevel tip. For example, the insertion numbers $41-44$ represent 4 insertions of a needle. For each insertion there are one rotation of 120° after a third and another rotation of 120° after two-thirds of the length. These 4 needles had been pushed in with an orthogonal force on the plastic hub in the direction of the bevel.

Insertion number	**Condition of insertion**	**Application of orthogonal efforts**
1 - 4	1 rotation of 180°	without
5 - 8	1 rotation of 180°	in the direction of bevel
9 - 12	1 rotation of 180°	in the orthogonal direction to bevel
13 - 16	1 rotation of 90°	without
17 - 20	1 rotation of 90°	in the direction of bevel
21 - 24	1 rotation of 90°	in the orthogonal direction to bevel
25 - 28	2 rotation of 180°	without
29 - 32	2 rotation of 180°	in the direction of bevel
33 - 36	2 rotation of 180°	in the orthogonal direction to bevel
37 - 40	2 rotation of 120°	without
41 - 44	2 rotation of 120°	in the direction of bevel
45 - 48	2 rotation of 120°	in the orthogonal direction to bevel
49	1 rotation of 180°	significant in the direction of bevel
50	1 rotation of 90°	significant in the direction of bevel
51	2 rotation of 180°	significant in the direction of bevel
52	2 rotation of 120°	significant in the direction of bevel
53 - 54	5 steps of insertion	without
55 - 56	5 steps of insertion	in the direction of bevel
57 - 58	5 steps of insertion	without
59 - 60	5 steps of insertion	in the direction of bevel
61 - 62	5 steps of insertion	in the orthogonal direction to bevel

Table 1: Description of the conditions of needle insertion. The first column gives the number of the insertion. The conditions of insertion are given in the second column, which could be one or two rotations after different lengths of insertion with an associated angle of rotation. The last column gives the orthogonal forces applied to the proximal extremity of the needle, which could be in the same direction or orthogonal to the bevel. For example, the insertion numbers $41 - 44$ represent 4 insertions of a needle. For each insertion there are one rotation of 120° after a third and another rotation of 120° after two-thirds of the length. These 4 needles had been pushed in with an orthogonal force on the plastic hub in the direction of the bevel.

2.2.2. Theoretical simulations and needles (TH needles)

'TH needles' were used with the aim of validating the force basis and evaluating its robustness. A classical static force scenario was chosen as being

that corresponding to the model most often encountered in the literature; a single force applied at the distal extremity of the needle, as illustrated in figure 5(a). In this model, it was assumed that the trajectory of the needle through the tissue is primarily dependent on forces on the bevel tip (Alterovitz et al., 2005; Webster et al., 2006; Duindam et al., 2010). Different boundary conditions can be added to generate other curvatures and to reveal inflection points as illustrated in figure 5(b). Lastly, a distributed force was proposed to change the mathematical degree of needle deflection in beam theory as shown in figure 5(c).

These TH needle trajectories were determined according to the equation (1). They were then segmented and registered by the same methods used for the PI needle including a segmentation error, and placed in the same reference frame.

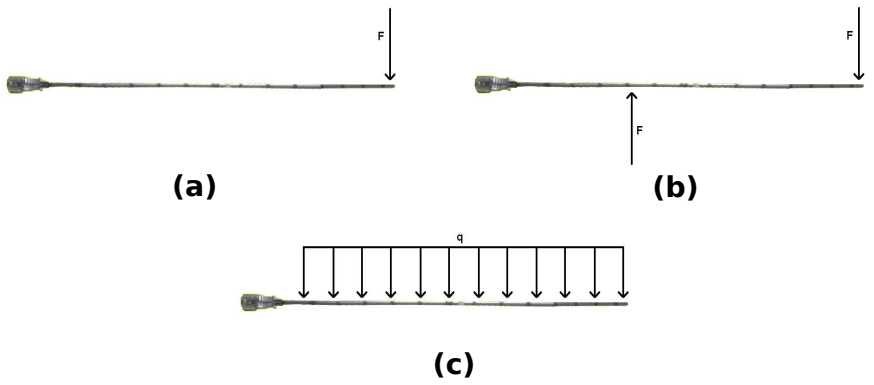

Figure 5: TH needles. *a*) Concentrated radial force, *b*) Two concentrated radial forces, *c*) Force distributed along the whole length of the needle. The TH simulations were used to validate the relevance of the force basis and its robustness.

2.2.3. Patients and needles (PA needles)

A clinical trial was performed at Grenoble University Hospital involving CT-guided interventional radiological procedures such as biopsies, injections, etc. The clinical trial was authorized by AFSSaPS (now ANSM), the relevant French regulatory authority for biomedical research and by the Comité de Protection des Personnes Sud-Est V, a French institutional review board

(ClinicalTrials.gov identifier: NCT00828893). Twenty series of CT-images of needles being inserted into patients were recorded. In contrast with the needle used in the pig shoulder studies, neither geometric data (radius, length) nor the material characteristics (Young modulus) of the needles used in this clinical trial were recorded. Furthermore, the conditions of insertion were not logged, as the data were acquired to evaluate the force basis for any type of needle, irrespective of whether its mechanical properties or the conditions of insertion are known.

3. Results

In this section, the results of the construction of the force basis are presented. The results of needle trajectory reconstructions, using this basis, are shown for some trajectories (chosen to highlight the different possible deformations and mispositionning) as well as the all trajectory reconstruction errors.

3.1. Construction of the force basis

Figure 6 shows, for each mode, the eigenvalues, the inertia and the cumulated inertia, associated with the 18 principal modes according to 2.1.5. For the deflected needle model, 95% of the variability in the training set could be explained using the first nine of the 18 basis modes ($p = 9$).

Figure 7 illustrates the distribution of the b_i (cf. 2.1.5) parameters of the deformable model for the i^{th} principal deformation mode of the model for each needle trajectory. By applying the upper limits, it is ensured that the shape / moment / forces generated are similar to those in the original training set. At these upper limits, the shape / moment / forces of the principle modes are shown in figure 8 (modes 1 to 3), figure 9 (modes 4 to 6) and figure 10 (modes 7 to 9). Each mode presents a complex form with different curvatures in the two planes $P1$ and $P2$. Furthermore, none of them corresponds to a simple force applied to the needle extremity.

3.2. Criteria for validating the quality of trajectory reconstruction and results

The performance of the force basis was checked on the entire needle dataset (PI needle (cf. section 2.2.1), TH needles (cf. section 2.2.2) and PA needles (cf. section 2.2.3)) presented in the study. Each shape was rebuilt from the basis in the two planes, $P1$ and $P2$ (cf. section 2.1.2). As previously described in paragraph 2.1.5, in order to interpret a new needle trajectory, the parameters which best match the reconstructed needle trajectory with the segmented needle trajectory must be found. The Euclidean distance between these two was minimized to obtain the coefficients of the force basis linear combination. All of the following figures (12 to 19) show some of the reconstructed needles trajectories. The points represent the segmentation of the needle trajectory as indicated in the paragraph 2.1.2. The reconstruction of the needle trajectory, i.e. the optimal linear combination of the force basis is represented by the dashed lines. For each of the following cases, reconstruction errors $([Q2, Q3], Max_{tip})_{P1,P2}$ were calculated in (mm) and in (‰) in the two planes $P1$ and $P2$. $Q2$ and $Q3$ represent the median value and the upper quartile of all the errors along the needle trajectory. Max_{tip} represents the maximum error at the needle tip, where positionning is very important in percutaneous procedures. In figure 11, the first bar represents the median value (Q2) and the second one the upper quartile (Q3). The maximum values of the tip deflection errors for each situation are shown in the table of figure 11.

3.2.1. Results for PI needles trajectories

Figure 12 shows the reconstruction of 2 PI needle trajectories, which were used to determine the force basis. In figures 12(a) and 12(b), the importance of the initial modeling of the needle trajectory, i.e of the determination of the $P1$ and $P2$ planes, is emphasized. These planes cannot be inverted. Indeed, the reconstruction in figure 12(a) is carried out in the planes $P1$ and $P2$, defined for data registration (cf. section 2.1.2) whereas in figure 12(b), these planes are inverted resulting in an aulty reconstruction. In figure 12(c), another PI needle trajectory is shown with a reconstruction in the correct planes. The reconstruction errors (‰) for all PI needle trajectories are shown in figure 11(a) and figure 11(b) for $P1$ and $P2$ respectively:

$([1.64, 2.11], 2.64)_{P1}$, $([0.83, 1.16], 4.45)_{P2}$.

3.2.2. Results for TH needles

Reconstructions of the three simulated TH needle trajectories are presented in figure 13. The reconstruction errors (‰) for all TH needle trajectories are shown in figure 11(e) and figure 11(f) for $P1$ and $P2$ respectively: $([4.01, 4.30], 3.70)_{P1}$, $([0.88, 1.15], 0.93)_{P2}$.

3.2.3. Results on in-vivo human tissue (PA needles)

While the material properties of the PI needles were known, this was not the case for the in-vivo observations on human. Nevertheless, it was possible to accurately reconstruct the needle deflection for needles with different lengths and different diameters. Two reconstructions are shown in figure 14. The errors in these reconstructions (‰) of PA needles are shown in figure 11(c) and figure 11(d) for $P1$ and $P2$ respectively: $([0.81, 1.19], 3.78)_{P1}$, $([0.40, 0.42], 1.21)_{P2}$.

4. Discussion

Model parameters

B-spline basis functions were used to model the shape of the needle trajectories from 3D segmentations of CT scans. This mathematical tool is useful to interpolate and to smooth a set of 3D points in order to obtain a representative shape that resembles reality.

The weights u_0, u_1, w_i in the B-spline model were chosen to be equal to 1. The τ parameter with a value of 100 was a good compromise between the interpolation and the smoothness qualities of the cubic B-spline functions. These weightings were chosen empirically at these values at the beginning of this study after the registration of some known cases. The choice of these

values seems adequate as the results of the reconstructions are accurate.

The roles of the two orthogonal planes ($P1$ and $P2$) defined in 2.1.2 are important. The first plane $P1$ represents the plane of greatest deflection. The second plane $P2$, orthogonal to $P1$, represents the secondary curves. These two planes cannot be inverted. If this is done as shown in 3.2.1(b), it results in an inaccurate reconstruction of the needle trajectory.

The use of PCA allows the principal variation modes to be identified. These are the most representative of the plausible variations in the needle's trajectory and thus give a compact representation of allowable variations. Indeed, an 18 vector basis was simplified down to a basis with 9 meaningful vectors.

Accuracy of reconstruction

Clinical studies show that errors in needle placement are due to several causes, such as human error, imaging limitations, target uncertainly, tissue deformation and needle deflection. The acceptable tolerance for the accuracy of needle insertion in clinical practice depends on the application. In fact, millimetric accuracy is required in procedures such as biopsies (prostate, liver, breast and kidney) while sub-millimetric accuracy is needed in brain or fetal procedures (Van Gerwen et al., 2012). These tolerances are used to evaluate the quality of the reconstructions.

To show that the built force basis was robust, reconstructions of theoretical simulations were presented. Indeed, 75% of the errors are under 4.30‰ ($0.86mm$), 1.15‰ ($0.23mm$) for $P1$ and $P2$ respectively. These results show the feasibility of reconstructing such simulations with very good accuracy.

In this paper, we also show that the force basis can be used to reconstruct needle deflection during real medical interventions in a pertinant way. The results show that 75% of the errors are under 1.19‰ ($0.24mm$), 0.42‰ ($0.08mm$) with a maximum error at the tip of 3.78‰ ($0.75mm$) and 1.21‰ ($0.24mm$) for $P1$ and $P2$ respectively. Moreover, we note that the errors obtained on the human studies are lower than those obtained with the experimental animal model, suggesting that the different methods of insertion performed on the pig shoulder were exhaustive enough to simulate an envi-

ronment representative of the clinical reality.

This force basis performs well in all reconstructions and is compatible with clinical practice and current medical devices that require sub-millimetric accuracy. In this study, the maximum error at the needle tip corresponds to a PI needle with an error of 4.45‰ ($0.89mm$).

Static approaches

During the insertion of a needle in percutaneous interventions using CT-guidance, the correct trajectory of the needle is checked by iterative CT images in order to prevent complications in the medical procedure if the anatomic structures are not as expected. Thus, such procedures require stepwise needle insertion and image acquisitions. This leads to a succession of static images of the needle. The static force assumption, encountered in clinical practice, could therefore provide a better approach for understanding real needle behavior and needle deflection models. The advantage of this approach, over the dynamic approaches, is that it allows friction and axial forces to be disregarded in the study of the needle-tissue interactions. This is confirmed by the experiments performed by Misra et al. (2010) which indicated that the effect of friction forces was minimal and can thus be neglected in some model.

As an illustration of these remarks we refer to the results presented in table 1, needles insertions 53 to 62 were in five steps as in a clinical procedure under CT guidance i.e. with several static stages. For these 10 insertions, the reconstructed intermediate trajectories are shown in figure 15. It can be seen that the part of the needle trajectory already made does not change in a consistent way during the successive stages of insertion. This confirms a significant amount of work by other groups, which assumes that the trajectory of the needle through the tissue is primarily dependent on the path of the bevel tip (Alterovitz et al., 2005; Webster et al., 2006).

Comparison with other approaches

Misra et al. (2010) and Asadian et al. (2011) considered the dynamic forces involved during insertion. These forces depend on the depth of insertion. However, for the forces they consider, the pertinent parameters of the

model have to be fitted using experimental data from previous insertions. Such a process may be difficult to use in a real clinical environment.

DiMaio and Salcudean (2002), Crouch et al. (2005) and Dehghan et al. (2008) used indirect methods to reconstruct the depth dependent axial force distribution in artificial materials, based on external force and material displacement measurements. An indirect means of estimating the applied force distribution involves the measurement of the resulting tissue deformation using a grid of black dots that can be tracked by a camera as they move. If the relationship between applied forces or stresses and tissue displacement is known, then the distribution of the force applied along the needle shaft can be computed. In our study, an indirect method that employs beam theory is also used. Nevertheless, the force distribution along the entire length of the needle can be found and not only the axial force.

Kataoka et al. (2002) and Simone and Okamura (2002) performed experiments to measure the resultant force during needle insertion into biological materials using a force sensor mounted on the outside extremity of the needle in the direction of motion. However, the force depends on the tissue penetrated and has not been validated in other cases. In our work, the force basis comes from experiments on porcine tissue, and is generic enough to be used in a pertinent way on humans and in theoretical simulations.

Interest of this generic basis

In this work, the force basis was built from experiments on porcine tissue. Its robustness and genericity have been demonstrated by the possibility of reconstructing, with good accuracy, 3 TH simulated and 20 PA needle insertions in addition to the 62 PI needle insertions.

This study highlights that knowledge of needle deformation allows reconstruction of the forces at play by decomposition of the force basis, making it possible to avoid other computing methods, such as Finite Element Analysis.

Furthermore, this static force basis may be of use to optimize the position of strain gauges or sensors (Park et al., 2010; Yang et al., 2010) on an instrumented needle.

An instrumented needle capable of providing information about its trajectory thanks to sensors on its surface may be very useful. This would be particularly so for the development of systems that are able to track needle deformation and would contribute to the realization of medical interventions that are safer, less invasive and more efficient. Safer because the position and the deflection of the needle would be better known in real time without any additional imagery throughout the procedure. Less invasive because the number of attempts needed for the placement of a needle, which does not follow the planned trajectory, could be decreased. Moreover, the number of controls necessary to ensure the correct positioning of the needle and thus the amount of irradiation received by patients and medical staff during CT-guided procedures could be reduced. And lastly, more efficient, because of better positioning of the needle tip at its target.

Finally, the static force basis may be valuable to model predicted deformations in the wide variety of mediums that are encountered in real clinical situations.

5. Conclusion

In this paper, a generic force basis is presented that acts on needles inserted during a medical procedure using needle trajectory data collected from a total of 62 needle insertions into a pig's shoulder. The needle trajectory data was collected by segmenting and recording 3D points along the needle trajectory from CT-images. Then, using static Beam and B-spline theories and PCA, the force basis was determined. It genericity was then validated on theoretical simulations as well as on 20 needles inserted into human tissue during real clinical procedures.

6. Funding sources

This work was supported by French state funds managed by the ANR within the Investissements d'Avenir programme (Labex CAMI) under reference ANR-11-LABX-0004.

Abayazid, M., Roesthuis, R., Reilink, R., Misra, S., 2011. Integrating deflection models and image feedback for real-time flexible needle steering. IEEE transactions on robotics, pp.1-12.

Abolhassani, N., Patel, R., Moallem, M., 2007. Needle insertion into soft tissue: A survey. Medical Engineering & Physics, vol.29 (4), pp.413-431.

Alterovitz, R., Goldberg, K., Okamura, A., 2005. Planning for steerable bevel-tip needle insertion through 2D soft tissue with obstacles. Proceedings of the IEEE International Conference on Robotics and Automation (ICRA), pp.1640-1645.

Asadian, A., Kermani, M., Patel, R., 2011. An analytical model for deflection of flexible needles during needle insertion. IEEE/RSJ International Conference on Intelligent Robots and Systems (IROS), pp.2551–2556.

Asadian, A., Kermani, M., Patel, R., 2012. A novel force modeling scheme for needle insertion using multiple kalman filters. IEEE Transactions on Instrumentation and Measurement, vol.61 (2), pp.429-438.

Barbe, L., Bayle, B., De Mathelin, M., Gangi, A., 2007. In vivo model estimation and haptic characterization of needle insertions. International Journal of Robotics Research, vol.26 (11-12), pp.1283-1301.

Cootes, T., 2000. An introduction to active shape models. Image Processing and Analysis, pp.223-248.

Cootes, T., Taylor, C., 2001. Statistical models of appearance for computer vision. Imaging Science and Biomedical Engineering. University of Manchester, Manchester M 13.

Crouch, J., Schneider, C., Wainer, J., Okamura, A., 2005. A velocity-dependent model for needle insertion in soft tissue. Medical Image Computing and Computer-Assisted Intervention (MICCAI), pp.624-632.

Dehghan, E., Wen, X., Zahiri-Azar, R., Marchal, M., Salcudean, S., 2008. Needle-tissue interaction modeling using ultrasound-based motion estimation: Phantom study. Computer Aided Surgery, vol.13 (5), pp.265-280.

DiMaio, S., Salcudean, S., 2002. Simulated interactive needle insertion. Proceedings. 10th Symposium on Haptic Interfaces for Virtual Environment and Teleoperator Systems (HAPTICS), pp.344-351.

Duindam, V., Xu, J., Alterovitz, R., Sastry, S., Goldberg, K., 2010. Three-dimensional motion planning algorithms for steerable needles using inverse

kinematics. International Journal of Robotics Research, vol.29 (7), pp.789-800.

Hing, J.T. and Brooks, A.D. and Desai, J.P., 2007. A biplanar fluoroscopic approach for the measurement, modeling, and simulation of needle and soft-tissue interaction. Medical Image Analysis, vol.11, pp.62-78.

Hocking, G., Hebard, S., Mitchell, C., 2011. A review of the benefits and pitfalls of phantoms in ultrasound-guided regional anesthesia. Regional anesthesia and pain medicine, vol.36 (2), pp.162.

Kataoka, H., Washio, T., Chinzei, K., Mizuhara, K., Simone, C., Okamura, A., 2002. Measurement of the tip and friction force acting on a needle during penetration. Medical Image Computing and Computer-Assisted Intervention (MICCAI), pp.216-223.

Misra, S., Ramesh, K., Okamura, A., 2008. Modeling of tool-tissue interactions for computer-based surgical simulation: a literature review. Teleoperators and Virtual Environments, vol.17 (5), pp.463-491.

Misra, S., Reed, K., Schafer, B., Ramesh, K., Okamura, A., 2010. Mechanics of flexible needles robotically steered through soft tissue. The International Journal of Robotics Research, vol.29 (13), pp.1640.

Okamura, A., Simone, C., O'Leary, M., 2004. Force modeling for needle insertion into soft tissue. IEEE Transactions on Biomedical Engineering, vol.51 (10), pp.1707-1716.

Park, Y., Elayaperumal, S., Daniel, B., Ryu, S., Shin, M., Savall, J., Black, R., Moslehi, B., Cutkosky, M., 2010. Real-time estimation of 3-d needle shape and deflection for MRI-guided interventions. IEEE/ASME Transactions on Mechatronics, vol.15 (6), pp.906-915.

Podder, T., Clark, D., Sherman, J., Fuller, D., Messing, E., Rubens, D., Strang, J., Brasacchio, R., Liao, L., Ng, W., et al., 2006a. In vivo motion and force measurement of surgical needle intervention during prostate brachytherapy. Medical Physics, vol.33, pp.2915.

Podder, T., Sherman, J., Fuller, D., Messing, E., Rubens, D., Strang, J., Brasacchio, R., Yu, Y., 2006b. In-vivo measurement of surgical needle intervention parameters: a pilot study. 28th Annual International Conference of the IEEE Engineering in Medicine and Biology Society, pp.3652-3655.

Roesthuis, R., van Veen, Y., Jahya, A., Misra, S., 2011. Mechanics of needle-tissue interaction. IEEE/RSJ International Conference on Intelligent Robots and Systems (IROS), pp.2557-2563.

Simone, C., Okamura, A., 2002. Modeling of needle insertion forces for robot-assisted percutaneous therapy. IEEE International Conference on Robotics and Automation (ICRA), vol.2, pp.2085-2091.

Van Gerwen, D., Dankelman, J., van den Dobbelsteen, J., 2012. Needle–tissue interaction forces–a survey of experimental data. Medical engineering & physics, vol.34 (6), pp.665-680.

Washio, T. and Chinzei, K., 2004. Needle force sensor, robust and sensitive detection of the instant of needle puncture. 7th International Conference on Medical Image Computing and Computer-Assisted Intervention (MICCAI), vol.3217, pp.113-120.

Webster, R., Kim, J., Cowan, N., Chirikjian, G., Okamura, A., 2006. Nonholonomic modeling of needle steering. The International Journal of Robotics Research, vol.25 (5-6), pp.509-525.

Yang, W., Bonvilain, A., Alonso, T., Moreau-Gaudry, A., Basrour, S., 2010. Modelling and characterization of an instrumented medical needle in sight of new microsensor design for its insertion guidance. Annual International Conference of the Engineering in Medicine and Biology Society (EMBC), pp.6465-6468.

Number mode	Eigenvalues	Inertia (%)	Cumulated Inertia (%)
1	5,2376	29,1	29,1
2	4,3487	24,2	53,3
3	2,0398	11,3	64,6
4	1,8262	10,1	74,7
5	1,0531	5,85	80,55
6	0,96552	5,4	85,95
7	0,65481	3,6	89,55
8	0,48279	2,7	92,25
9	0,45974	2,55	94,8
10	0,38816	2,2	97
11	0,20356	1,1	98,1
12	0,12255	0,7	98,8
13	0,098337	0,5	99,3
14	0,063473	0,35	99,65
15	0,048524	0,3	99,95
16	0,0041963	0,02	99,97
17	0,0016324	0,009	99,98
18	0,0012362	0,007	100

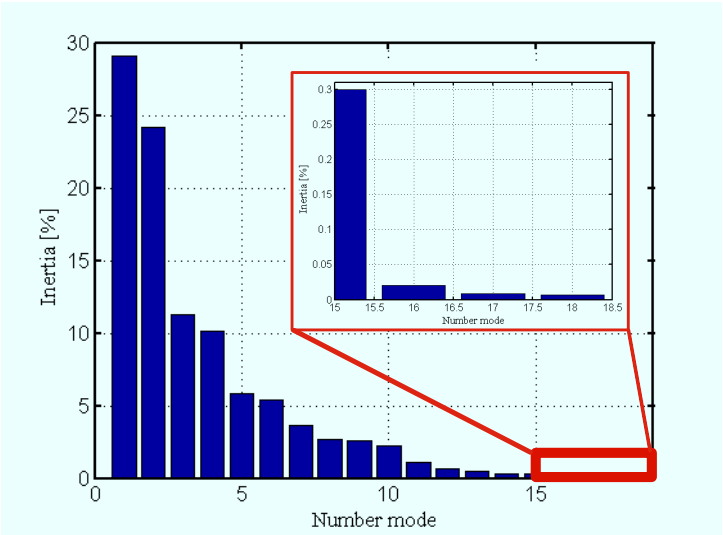

Figure 6: Eigenvalues and inertia determined by PCA. For each mode, the eigenvalues, the inertia and the cumulated inertia, associated with the 18 principal modes according to 2.1.5 are presented.

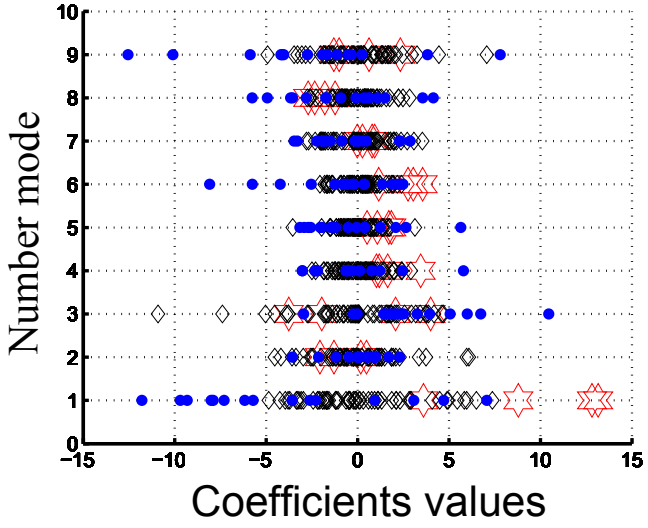

Figure 7: Visualization, for all needle insertions, of the coefficients of distribution for the first nine principal modes. 3 TH needles (stars), 62 PI needles (diamonds) and 20 PA needles (circles)

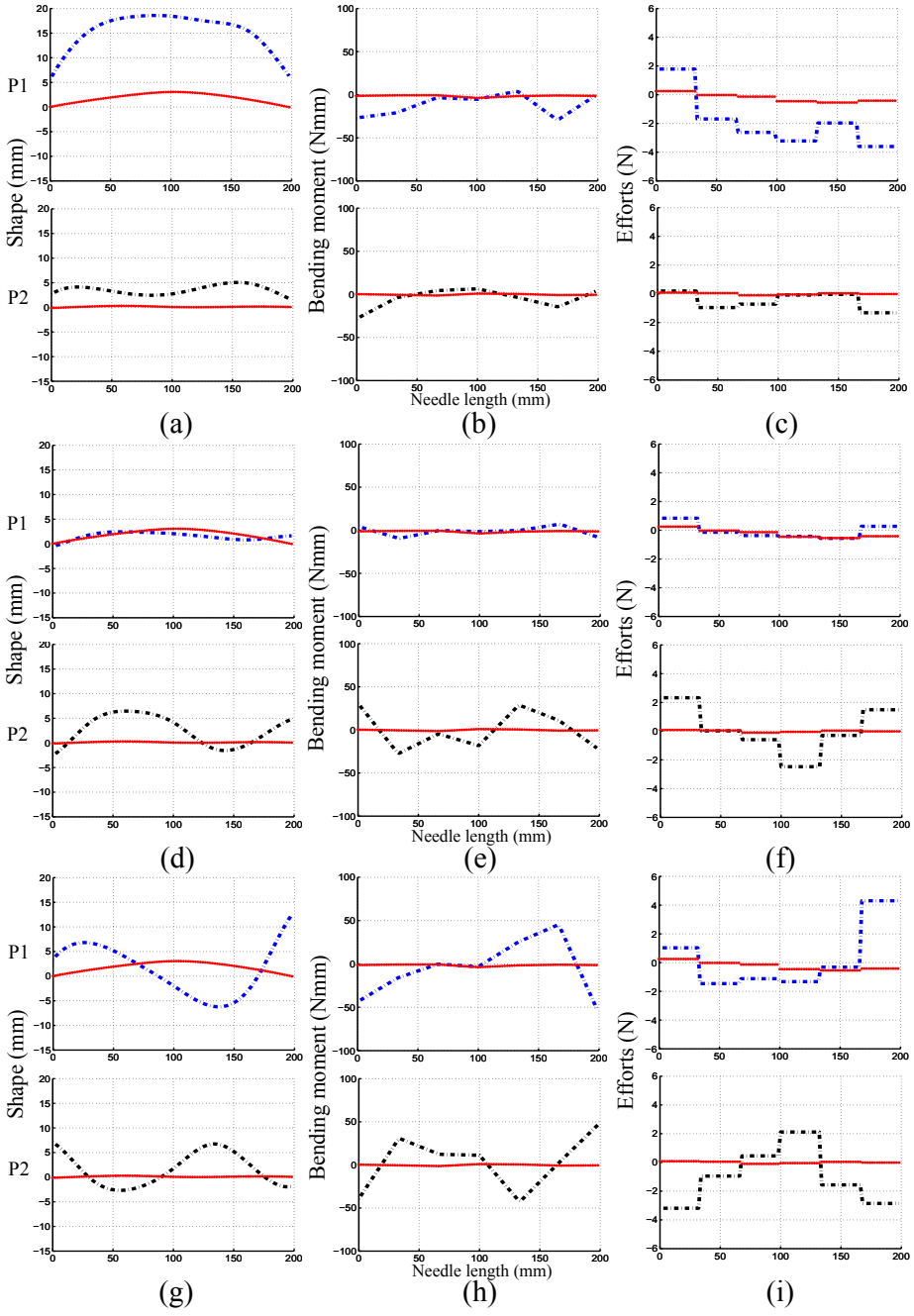

Figure 8: Effect of varying each of first three needle models' shape (mm) / moment (Nmm) / force(N) parameters in turn between given limits. Each pad shows the effect of varying one of the shape parameters (or moment or forces) keeping the others at zero for the two planes along the needle (0-200 mm). The median points are the mean shape / moment / force.

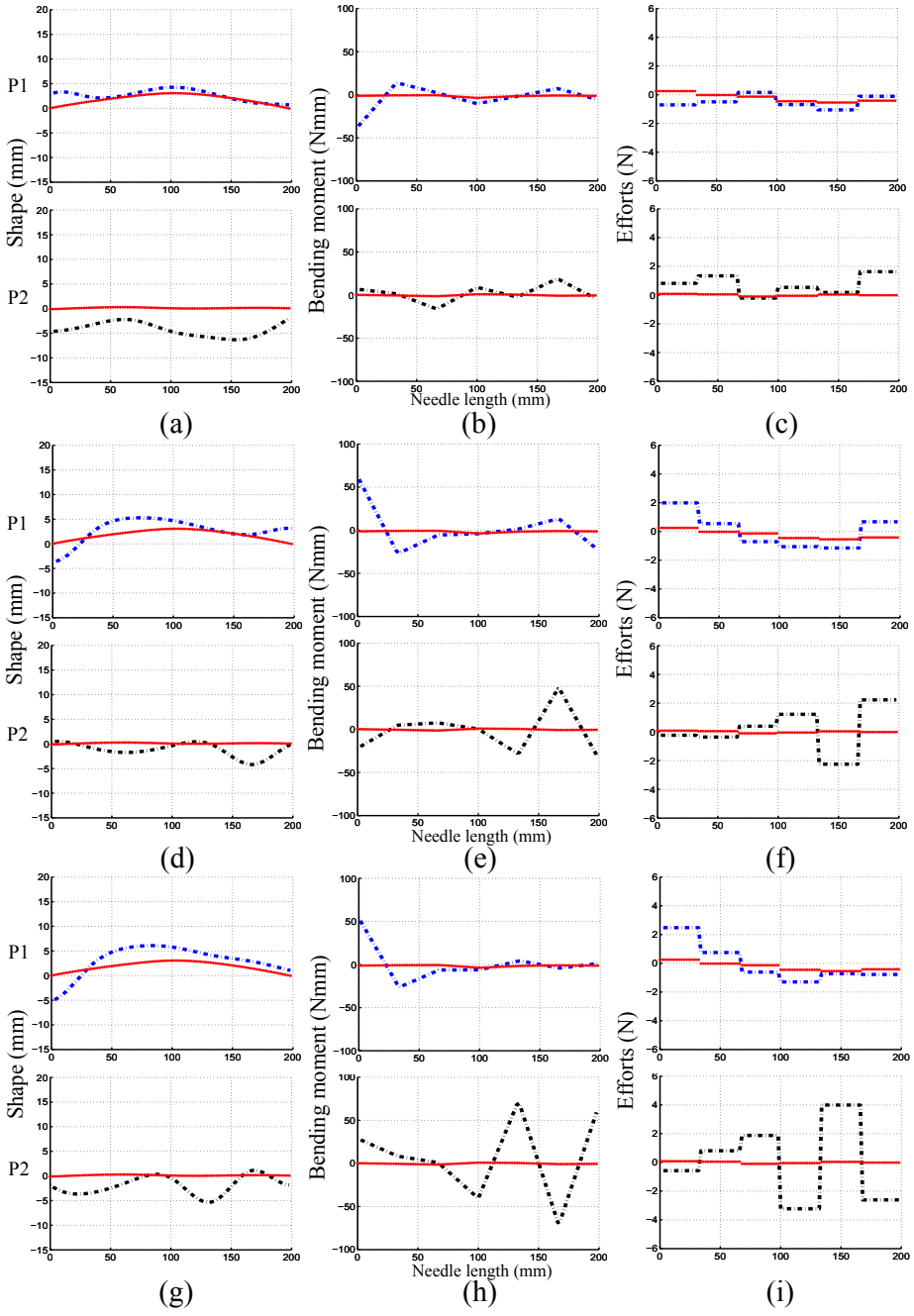

Figure 9: Effect of varying from the fourth to the sixth needle models' shape (mm) / moment (Nmm) / force (N) parameters in turn between given limits. Each pad shows the effect of varying one of the shape parameters (or moment or forces) keeping the others at zero for the two planes along the needle (0-200 mm). The median points are the mean shape / moment / force.

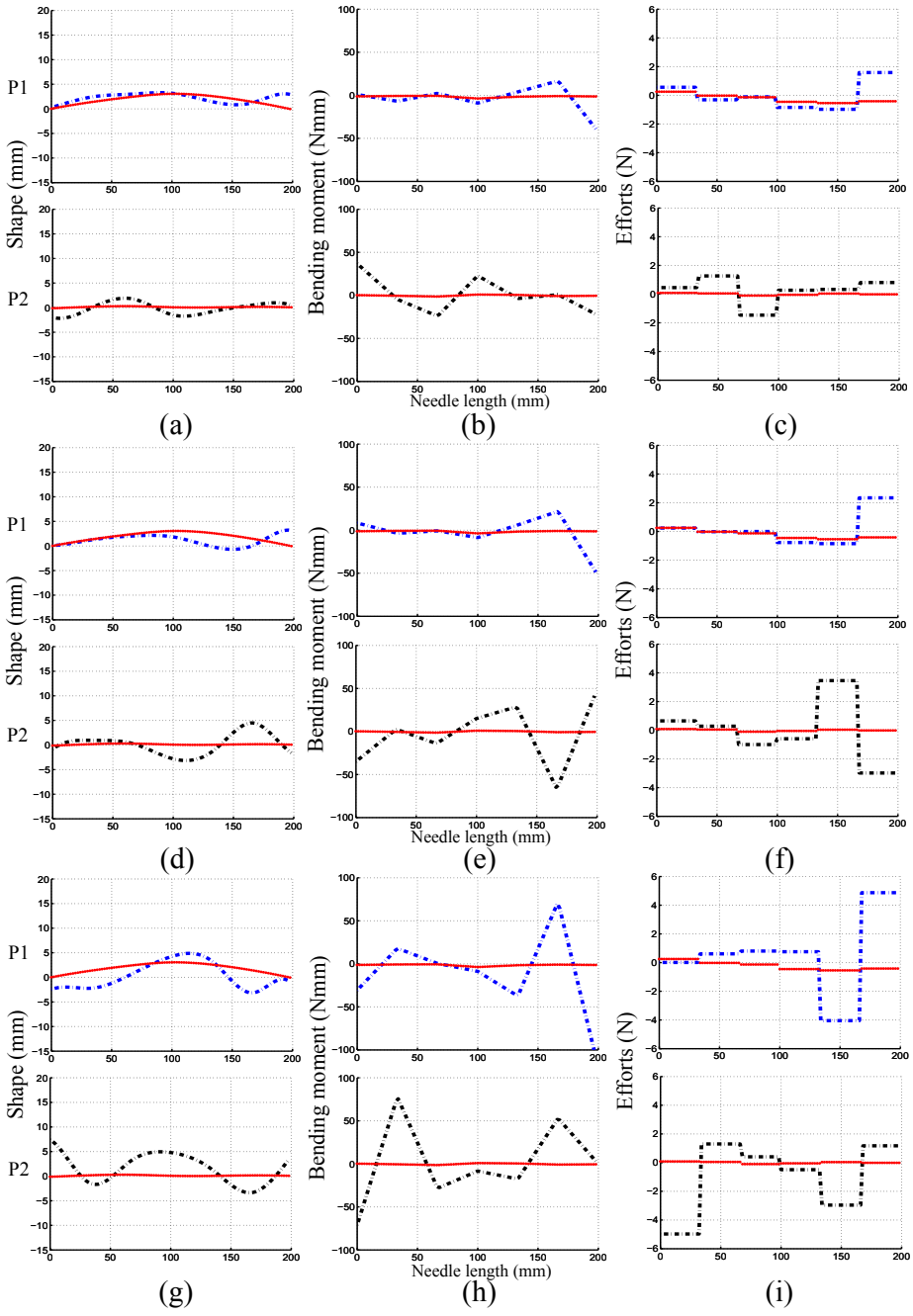

Figure 10: Effect of varying the last three needle models' shape (mm) / moment (Nmm) / force (N) parameters in turn between given limits. Each pad shows the effect of varying one of the shape parameters (or moment or forces) keeping the others at zero for the two planes along the needle (0-200 mm). The median points are the mean shape / moment / force.

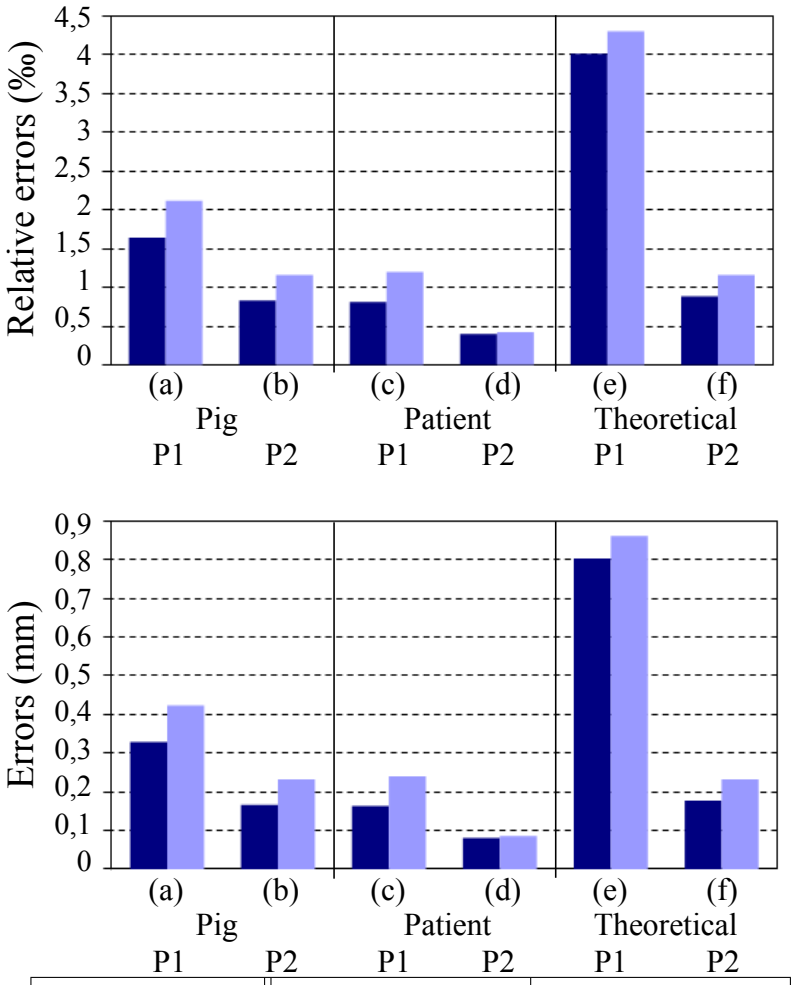

	Max_{tip} **(mm)**	Max_{tip} (‰)
PI needle: P1	0,53	2,64
PI needle: P2	0,89	4,45
PA needle: P1	0,75	3,78
PA needle: P2	0,24	1,21
TH needle: P1	0,74	3,70
TH needle: P2	0,18	0,93

Figure 11: Reconstruction errors (‰) and (mm) in the two planes P1 and P2: first bar (median value (Q2)), second bar (upper quartile (Q3)). The table represents the maximum value of the tip errors. *a*) PI needle: P1, *b*) PI needle: P2, *c*) PA needles: P1, *d*) PA needles: P2, *e*) TH needles: P1, *f*) TH needles: P2.

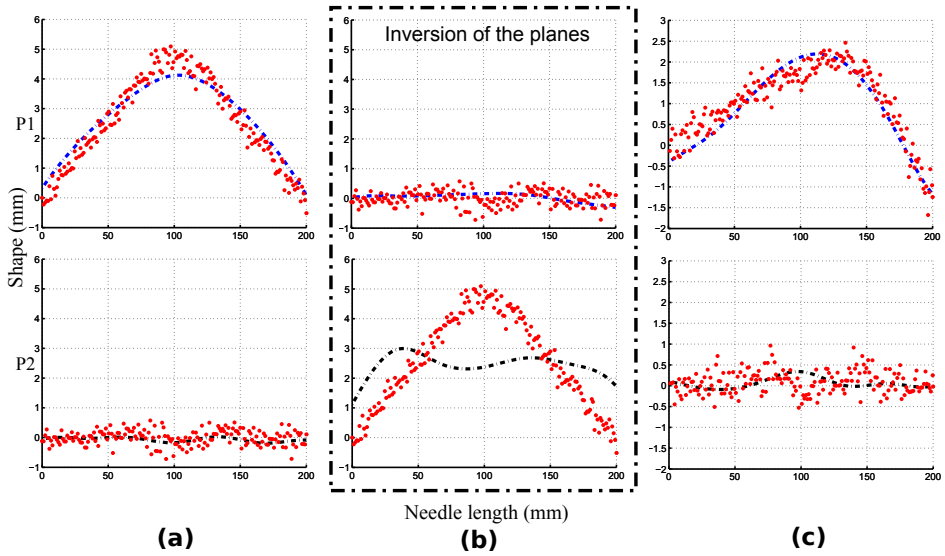

Figure 12: Deflection of PI needles: *a*) Needle trajectory 1 reconstruction in the correct planes P1 and P2, *b*) Needle trajectory 1 reconstruction when the planes P1 and P2 are reversed, *c*) Needle trajectory 21 reconstruction in the correct planes P1 and P2. The dots represent the segmented needle and the dashed lines represent the reconstructed needle trajectory using the force basis

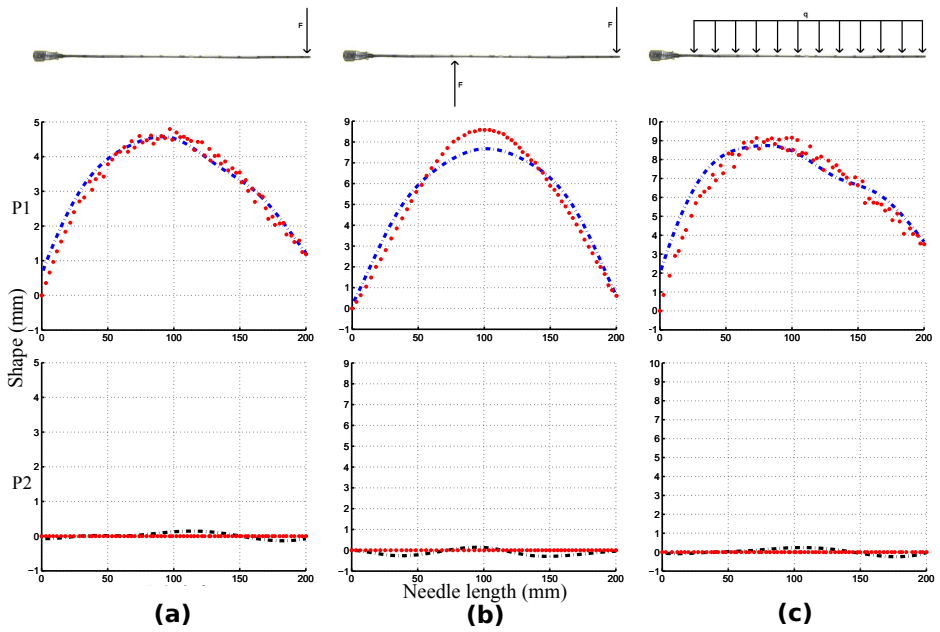

Figure 13: Reconstruction of TH needles deflections. *a*) Modeling in the case of concentrated radial forces in planes P1 and P2, *b*) Modeling in the case of two concentrated radial forces in planes P1 and P2, *c*) Reconstruction with constant force distribution in planes P1 and P2. The dots represent the segmented needle trajectory and the dashed lines represent the needle trajectory reconstructed using the force basis.

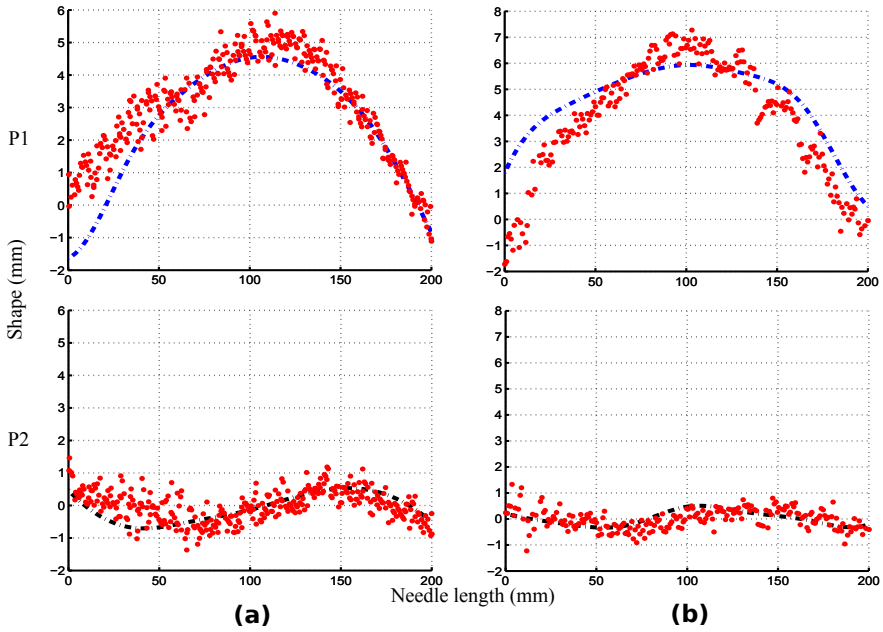

Figure 14: Deflection reconstruction of PA needles. *a*) Needle 1 in the planes P1 and P2, *b*) Needle 2 in the planes P1 and P2. The dots represent the segmented needle trajectory and the dashed lines represent the needle trajectory reconstructed using the force basis.

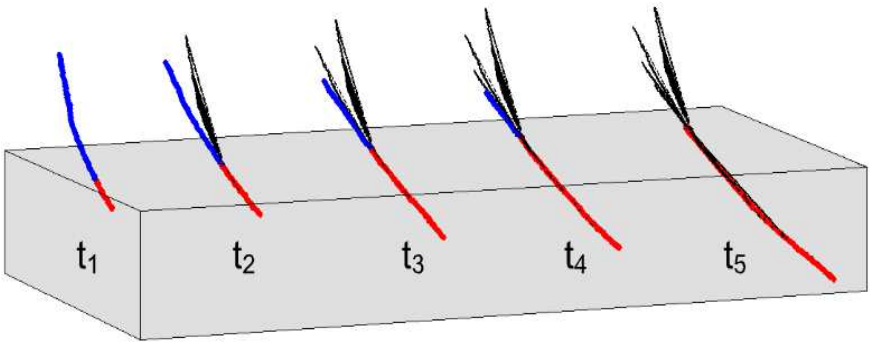

Figure 15: Successive construction of a needle's trajectory during the different steps of insertion (five insertion steps). Once inside the tissue, the needle maintains the same trajectory.